Check for updates

Enhancing orange-red emission by doping/codoping CsPb$_2$Br$_5$ with cations through a room-temperature aqueous-phase synthesis†

Yuwei Zhong, Xinran Li, Hao Zhang, Rong Zhang, Kaiwen Hu,*
Xuedong Zhou and Yi Xie (iD)*

Despite the rising advances in the field of all-inorganic CsPb$_2$Br$_5$-based materials and their photoelectronic applications, the exploitation of facile synthetic procedures and enhancement of optical properties remain challenging. Herein, we report a facile room-temperature aqueous phase synthesis of orange-red-emitting cation-doped and codoped CsPb$_2$Br$_5$ materials with enhanced photoluminescence (PL) performance and stability. Only a very weak broad PL peak at around 618 nm is observed in the undoped CsPb$_2$Br$_5$ microsheets. However, doping with Cu and codoping with Cu/Mn, Cu/Zn or Cu/Cd significantly enhance the PL intensity of the resulting CsPb$_2$Br$_5$-based samples. The stability of the representative Cu-doped and various codoped CsPb$_2$Br$_5$ samples is evaluated under various conditions such as soaking in water, high temperature up to 150 °C, and an ambient environment at room temperature. This work provides a facile and cost-effective path for large-scale and controlled synthesis of orange-red emissive CsPb$_2$Br$_5$-based materials with enhanced optical performances, excellent environmental stability, and potential in LEDs.

Introduction

All-inorganic lead halide perovskite CsPbX$_3$ (X = Cl, Br, and I) materials and their applications have attracted great attention of researchers due to their excellent optical and electrical properties.[1,2] However, the practical applications and further commercialization of CsPbX$_3$ materials are still seriously plagued by their poor stability towards moisture, air, heat and light. Therefore, searching for other cesium–lead–halide (Cs–Pb–X) derivative phases with good stability remains one of the most popular research topics in the related fields.

As one of the derivatives with the same constituent elements as CsPbBr$_3$ but varied stoichiometric ratios, CsPb$_2$Br$_5$ materials display different crystal structures and unique chemical–physical properties compared with CsPbBr$_3$.[3] Recently, two-dimensional (2D) CsPb$_2$Br$_5$ has emerged as one of the promising alternatives to CsPbBr$_3$ due to its good stability, versatility in the crystal structure, and excellent optoelectronic/optical properties. Zhang *et al.* reported the growth of CsPb$_2$Br$_5$ single crystals for fabricating high-performance deep UV photodetectors, which showed high

responsivity for deep-UV detection.[4] By combination with high-quality CsPbI$_3$ orthogonal phases, tetragonal CsPb$_2$Br$_5$ nanostructures have been explored in photovoltaic applications.[5] First principles calculations indicated that CsPb$_2$Br$_5$ is an indirect band gap semiconductor with a band gap of 3.05 eV.[6] Despite these investigations, there are many disputes about the intriguing emission mechanism of CsPb$_2$Br$_5$-related systems which needs to be further clarified.[3,6,7] For instance, as an indirect bandgap material, the luminescence of CsPb$_2$Br$_5$ is not expected to be very high, while many reported cases are different from that.[8] It is still important to fully understand the optical performances and structural characteristics of CsPb$_2$Br$_5$.

Significant efforts toward various synthetic strategies have been made to achieve CsPb$_2$Br$_5$ materials with controlled morphologies and optical properties and to explore their photoelectric applications.[9–11] Zhi *et al.* induced the synthesis of CsPb$_2$Br$_5$ nano/micro-sheets by an anti-solvent crystallization strategy in the presence of *N,N*-dimethylformamide (DMF), isopropanol (IPA) and toluene, and fabricated a CsPb$_2$Br$_5$-based photoconductive photodetector with a high specific detection rate and photoresponsivity.[12] Ruan *et al.* reported a mercaptan ligand-assisted procedure to directly synthesize 1D tetragonal CsPb$_2$X$_5$ (X = Cl, Br, I) nanowires with tuneable fluorescence peaks in the visible region, and the resulting nanowires exhibited good stability at high temperatures and high humidity.[10] By adjusting the cesium-to-lead ratio in the

State Key Laboratory of Silicate Materials for Architectures, Wuhan University of Technology, No. 122, Luoshi Road, Wuhan 430070, P. R. China.
*E-mail: hkw@whut.edu.cn, xiey@whut.edu.cn*

† Electronic supplementary information (ESI) available: Additional SEM images, XRD patterns, optical spectra, and elemental mapping. See DOI: https://doi.org/10.1039/d4ce00593g

Paper

presence of capping ligands such as oleic acid and oleylamine, different perovskite derivatives such as Cs_4PbBr_6, $CsPbBr_3$ and $CsPb_2Br_5$ with various dimensionalities were formed.[9] Tetragonal $CsPb_2Br_5$ nanosheets were achieved by a chemical transformation from cubic $CsPbBr_3$ nanocrystals with the assistance of the dodecyl dimethylammonium bromide (DDAB) ligand,[13] or by increasing the reaction time.[14] However, most preparation methods for $CsPb_2Br_5$ materials involved organic capping ligands/surfactants, or strict reaction conditions such as high temperature in a hot-injection procedure.[14] A scalable, green and environmentally friendly synthetic approach is desirable for $CsPb_2Br_5$ and is one of the interesting research directions at present.

Combining different Cs–Pb–Br derivatives has been verified to be an effective approach to enhance both stability and luminescence emission.[15] $CsPbBr_3$-embedded Cs_4PbBr_6 NCs as-synthesized through a room-temperature (RT) precipitation procedure could be further transformed into $CsPbBr_3$/$CsPb_2Br_5$ nanocomposites after treatment with water, which were demonstrated as efficient fluorescent probes in live HeLa cells.[15] A $CsPbBr_3$@$CsPb_2Br_5$ heterojunction was formed by partially converting $CsPbBr_3$ to $CsPb_2Br_5$ in the presence of a small amount of water, and the resulting $CsPbBr_3$@$CsPb_2Br_5$ composite could promote the carrier separation efficiency and thus exhibited better photocatalytic activity than pure $CsPbBr_3$.[16] Despite these great efforts and contributions, it is still of great value to obtain a pure $CsPb_2Br_5$ phase for further investigation since the coexistence of impurities (*e.g.*, $CsPbBr_3$ and Cs_4PbBr_6) displaying green emission usually cause widespread controversy.

Besides, partially or completely replacing Pb^{2+} in the Cs–Pb–X system with guest metal cations can eliminate the toxicity and improve the stability of the resulting materials.[17] Doping $CsPbX_3$ with various cations such as Mn^{2+}, Zn^{2+}, Sn^{2+}, Bi^{3+}, *etc.* has been explored to tune the band gap and enhance the optical and photophysical performances.[18–23] Dopants such as Mn^{2+}, Ni^{2+}, Cd^{2+}, and Zn^{2+} cations were used to proportionally substitute the B-site cation (*i.e.*, Pb^{2+}) of $CsPbBr_3$ and $CsPb_2Br_5$ using high-energy ball milling to obtain all-inorganic high-entropy dual-phase Cs(Pb–Mn–Ni–Zn–Cd)Br_3/Cs(Pb–Mn–Ni–Zn–Cd)$_2Br_5$) perovskite nanocrystals.[24] Mo-doped dual phase $CsPb_2(Cl_xBr_{1-x})_5$/$CsPb(Cl_xBr_{1-x})_3$ was prepared through a hot-injection procedure in the presence of oleylamine and octadecene.[25] Relatively, doping $CsPb_2Br_5$ with cations to tune or enhance the optical and chemical–physical performances was much less reported. Doping alkali metal cations (*e.g.*, K^+, Rb^+) into the non-emissive transparent $CsPb_2Br_5$ crystal induced a red emission with a broad peak in the resulting sample.[26]

In this work, we developed a facile and environment-friendly approach to synthesize cation-doped/co-doped $CsPb_2Br_5$ materials with enhanced optical performances through a RT aqueous ligand-free system (Scheme 1). This method avoids the use of organic capping ligands, versatile and toxic solvents, and high temperature reactions. By
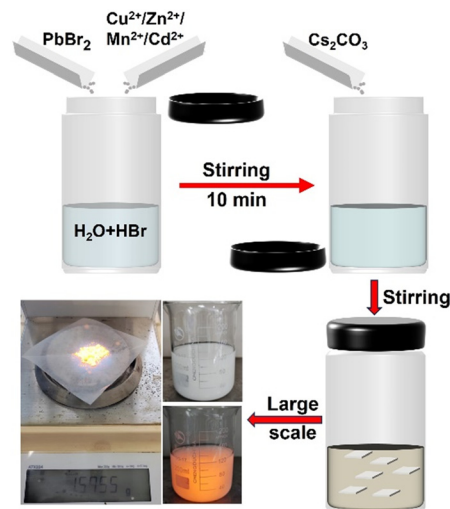
Scheme 1 Schematic illustration of the room-temperature aqueous phase synthesis of cation-doped/codoped $CsPb_2Br_5$ with enhanced orange-red emission.

optimizing the synthesis parameters, the representative doped sample maintained its stability under various conditions such as soaking in water for 30 days, being treated at high temperature up to 150 °C, and under an ambient environment.

Experimental

Chemicals and materials

Lead(II) bromide ($PbBr_2$, 99%), cupric bromide ($CuBr_2$, 99%), zinc bromide ($ZnBr_2$, 99.9%), and caesium carbonate (Cs_2CO_3, 99.9%) were purchased from Macklin. Manganese(II) chloride tetrahydrate ($MnCl_2 \cdot 4H_2O$, 99%) and hydrobromic acid (HBr, 48%) were purchased form Aladdin. Ethanol (AR) was purchased from Sinopharm, and cadmium bromide tetrahydrate ($CdBr_2 \cdot 4H_2O$, 99.5%) was purchased from Weng Jiang Reagent. All chemicals were used as received without any further purification.

Preparation of Cu-doped $CsPb_2Br_5$ and Cu–Mn-, Cu–Cd-, and Cu–Zn-co-doped $CsPb_2Br_5$

The preparation of all the samples was carried out at RT. In a typical synthesis of Cu-doped $CsPb_2Br_5$, a transparent light brown Pb–Cu-based complex solution was prepared first by dissolving 100 mg of $PbBr_2$ (0.27 mmol) and 15.1 mg of $CuBr_2$ (0.0675 mmol) in 6 mL solution containing 4.0 mL of H_2O and 2 mL HBr. Then, 90 mg (0.28 mmol) Cs_2CO_3 was added into the as-prepared transparent Pb–Cu-based complex solution under stirring. The colour of the dispersion turned immediately from light brown transparent to yellow, and then white precipitates were formed. The reaction was kept for additional 2 h, and the resulting white precipitates were washed twice with water and one more time with ethanol, followed by centrifugation and drying at RT to obtain the orange-red-emissive Cu-doped $CsPb_2Br_5$ powder. The various

cation-codoped $CsPb_2Br_5$ materials were synthesized using the same procedure except that other cation precursors such as $MnCl_2 \cdot 4H_2O$, $ZnBr_2$, or $CdBr_2 \cdot 4H_2O$ were added together with $CuBr_2$. For comparison, undoped white $CsPb_2Br_5$ powder with weak orange-red emission was also prepared in the absence of any guest cations (*i.e.*, Cu^{2+}, Mn^{2+}, Zn^{2+}, and Cd^{2+}).

Material characterization

The morphology, energy dispersive X-ray spectra (EDS) and elemental mapping analyses of the samples were analysed using scanning electron microscopy (SEM, QUANTA FEG 450). High-resolution transmission electron microscopy (HRTEM) images were acquired on a JEM 2100F (JEOL, Japan) microscope equipped with a field emission gun working at 200 kV accelerating voltage. The samples were prepared by drop-casting particle dispersions on 300 mesh Cu grids covered with an ultrathin amorphous carbon film, followed by placing in a high vacuum pumping station to let the solvent completely evaporate. The phase of the sample was analysed in air on a Bruker D8 Advanced X-ray diffractometer (XRD) equipped with a 1.8 kW CuKα ceramic X-ray tube, operating at 40 kV and 40 mA. The XRD patterns were collected in the Bragg–Brentano parafocusing geometry with a step size of 0.02°. The ultraviolet-visible diffuse reflectance spectra (UV-vis DRS) of the powder samples were recorded on a UV-2600 UV-vis-NIR spectrophotometer (Shimadzu, Japan) equipped with a diffuse reflector. The samples for steady-state PL measurements were prepared by casting the as-synthesized particle dispersion on glass slides and drying at RT. The test was performed on a fluorescence spectrophotometer (TM/QM/NIR, PTI, USA) by exciting the samples at 365 nm.

Results and discussion

Characterization of cation-doped and codoped $CsPb_2Br_5$

The RT procedure has been verified to be an efficient and facile approach for low-cost and large-scale production of perovskite-based materials.[27–30] In order to optimize the RT procedure to obtain cation-doped/codoped $CsPb_2Br_5$ with improved optical properties, we first of all collected a series of undoped $CsPb_2Br_5$ samples by changing the reaction time and monitored the evolution of their spectral absorbance, PL spectra and crystal structure (black curves in Fig. 1a and b, see detailed information in Fig. S1 of the ESI†). The UV-visible diffuse reflectance spectra of the undoped $CsPb_2Br_5$ materials are shown in Fig. S1a† and 1a (black solid curve). All samples display two absorption peaks at around 308 nm and 340 nm, with absorption edges at around 325 nm and
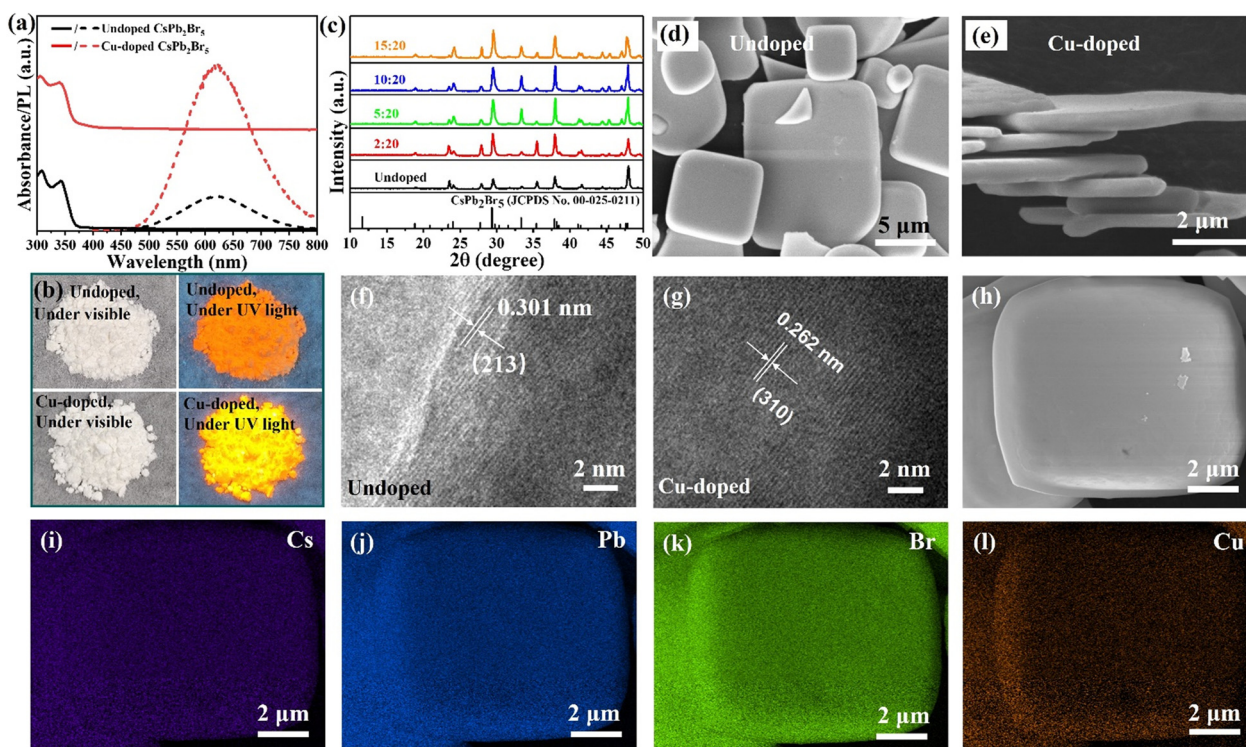

Fig. 1 (a) UV-visible diffuse reflectance spectra (solid lines) and PL spectra (dashed lines) of the representative undoped $CsPb_2Br_5$ (black curves) and Cu-doped $CsPb_2Br_5$ (red curves). (b) Digital photographs of the undoped and Cu-doped $CsPb_2Br_5$ powders under visible and UV light, respectively. (c) XRD patterns of the undoped $CsPb_2Br_5$ and Cu-doped $CsPb_2Br_5$ as-synthesized in the presence of different amounts of Cu precursor (denoted as the precursor molar ratio of Cu : Pb). (d and e) SEM images of the undoped $CsPb_2Br_5$ (d) and the representative Cu-doped $CsPb_2Br_5$ samples (e). (f and g) HRTEM images of the undoped $CsPb_2Br_5$ (f) and Cu-doped $CsPb_2Br_5$ (g), respectively. (h–l) High-magnification SEM image (h) and corresponding EDS element mapping images (i–l) of the representative Cu-doped $CsPb_2Br_5$.

370 nm, corresponding to energy gaps of 3.82 eV and 3.35 eV, respectively. In addition, an obvious absorption peak at around 519 nm is observed for the samples collected within 1 h of reaction, yielding an energy gap of ~2.32 eV. By prolonging the reaction time to 1.5 h and 2 h, the absorption at around 519 nm vanished. The PL spectra of the undoped $CsPb_2Br_5$ samples formed at different times are reported in Fig. S1b and c of the ESI.† The samples collected within 1 h displayed strong green emission at around 524 nm and relatively weak orange-red emission at around 618 nm (see the magnified view in Fig. S1c of the ESI†). As the reaction time prolonged, the PL peak at around 618 nm became relatively stronger in comparison with the peak at around 524 nm. Only an orange-red emission peak was observed after 2 h of reaction, which can be visible by the comparison of the digital photographs of the related powder samples under UV irradiation (insets in Fig. S1b†).

The experimental XRD patterns and SEM images of the undoped samples obtained at different reaction times are provided in Fig. S1d and S2 of the ESI† (see also the black curve in Fig. 1c and d). The diffraction peaks of all the undoped samples matched well with the tetragonal $CsPb_2Br_5$ phase (JCPDS No. 00-025-0211), which is in agreement with previously reported $CsPb_2Br_5$,[4,31,32] without any impurity peaks detected in the samples. The three sharp diffraction peaks at 2θ of 23.4°, 35.5°, and 47.9° can be assigned to the (210), (312), and (420) crystal planes of the tetragonal $CsPb_2Br_5$ phase, respectively. The absence of impurity peaks indicated the high crystalline quality of the as-prepared $CsPb_2Br_5$. We noticed that the peak at $2\theta = 11.8°$, widely reported for $CsPb_2Br_5$ crystals and indexed to the (002) plane,[6,33] is weak (e.g., for samples formed at 30 and 60 min) or absent (e.g., for samples collected at 1.5 h and 2 h) in our case. As shown from the SEM images, the orange-red emissive undoped $CsPb_2Br_5$ is microsheets (Fig. 1d and S2 of the ESI†).

The previously reported optical performances of $CsPb_2Br_5$ materials indicated many controversial and interesting results. Combination of the experimental results with density functional theory (DFT) calculation analyses indicated an indirect band gap characteristic and a green emission feature in $CsPb_2Br_5$ single crystals.[4] Green PL emission was also observed on $CsPb_2Br_5$ nanoplatelets synthesized by a facile precipitation reaction[34] and $CsPb_2Br_5$ nanowires and nanosheets achieved from alkyl-thiol-induced transformation of $CsPbBr_3$ nanocubes.[35] However, Chen et al. focused on individual $CsPb_2Br_{5-\gamma}X_\gamma$ (X = Cl, I) nanowires and noticed that the green PL emission came from the discrete $CsPbBr_{3-\gamma}X_\gamma$ nanocrystals on the nanowires instead of the whole body of nanowires, confirming that $CsPb_2Br_{5-\gamma}X_\gamma$ nanowires had no green emission.[36] Based on experimental and DFT simulation results, Li et al. presented that $CsPb_2Br_5$ nanosheets only exhibited a large indirect band gap of 2.979 eV and were PL-inactive.[11] However, $CsPb_2Br_5$ nanocrystals obtained by a green wet chemical approach displayed orange emission centered at 601 nm.[37] It is noteworthy that the PL emissions

in the yellow and red spectral region were observed for APb_2Br_5 crystals (A = K, Rb) at a low temperature of 8 K.[38] A similar observation was reported on $CsPb_2Br_5$ single crystals at temperature below 170 K, which is possibly related to the radiative relaxation of electronic excitations involving lattice defects or impurity centers.[4]

In our case, the absorption peak at around 519 nm of the undoped Cs–Pb–Br intermediates collected within 1 h is in accordance with the previously reported optical features of $CsPb_2Br_5$.[12,39,40] It is interesting that the undoped $CsPb_2Br_5$ and the cation-doped and codoped $CsPb_2Br_5$ materials that will be discussed in the following sections display unique orange-red PL emission at around 618 nm at RT, which might originate from lattice defects as that previously reported on $CsPb_2Br_5$ at low temperature.[4] However, we cannot provide more detailed explanation on the orange-red emission at this moment since it requires further investigation in future work.

It is noteworthy that the intensity of the orange-red emission of the $CsPb_2Br_5$ materials can be significantly increased to 4.7 times upon doping with Cu; meanwhile, no significant shift of the emission wavelength can be observed (dashed curves in Fig. 1a, see also Fig. S3a of the ESI†). The enhancement of the orange-red emission can be also directly visualized by the digital photographs of the Cu-doped $CsPb_2Br_5$ powder under UV irradiation (Fig. 1b). By analogy to that of the undoped $CsPb_2Br_5$, the UV-visible DRS spectra of the Cu-doped $CsPb_2Br_5$ samples display two optical absorption peaks at around 309 nm and 341 nm, respectively (solid curves in Fig. 1a, see also Fig. S3b of the ESI†). The comparison of other characterization methods such as crystal phase, morphological property and elemental analyses between the undoped and the Cu-doped $CsPb_2Br_5$ samples is reported in Fig. 1c–l and S3–S5 of the ESI.† As shown in Fig. 1c, doping $CsPb_2Br_5$ with Cu did not remarkably alter the crystal structure. The diffraction pattern is in good agreement with that of tetragonal phase $CsPb_2Br_5$ (JCPDS No. 00-025-0211). For details, the diffraction peaks at 2θ of 23.5°, 24.1°, 27.8°, 29.4°, 33.4°, 35.5°, 38.0°, and 47.9° correspond to the (210), (202), (114), (213), (310), (312), (313), and (420) directions of $CsPb_2Br_5$, respectively. A closer look at the magnified view of the XRD peak corresponding to the (213) crystal plane indicates a slight shift to a larger angle when increasing the Cu^{2+} amount in the precursors (denoted as the precursor molar ratio of Cu : Pb, Fig. S3c in the ESI†). SEM images were provided to compare the morphologies of the undoped and Cu-doped $CsPb_2Br_5$ obtained with different Cu-precursor amounts (Fig. 1d and e, S4 of the ESI†). The morphology of the Cu-doped samples with a low dose of Cu^{2+} dopant (e.g., Cu : Pb ratio below 1 : 5) was still maintained as microsheets (Fig. 1d and e, and S4a and b†), while increasing the Cu-precursor amount led to the formation of smaller cube-like and rod-like particles (Fig. S4c and d in the ESI†). Fig. 1f and g show the HRTEM images of the undoped and typical Cu-doped $CsPb_2Br_5$
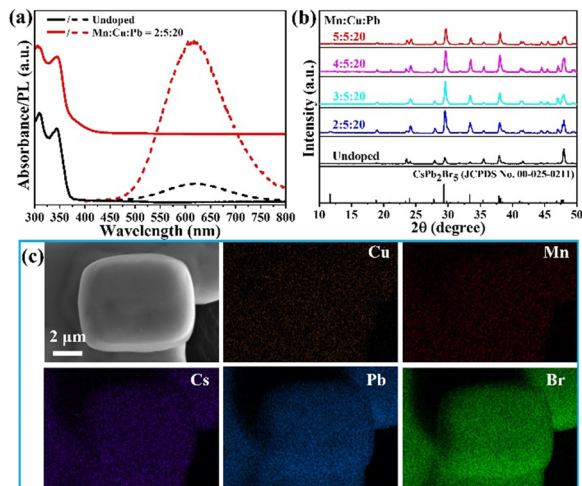
Fig. 2 (a) UV-visible diffuse reflectance spectra (solid lines) and PL spectra (dashed lines) of the undoped $CsPb_2Br_5$ (black curves) and typical Cu–Mn-codoped $CsPb_2Br_5$ (red curves). (b) XRD patterns of the Cu–Mn-codoped $CsPb_2Br_5$ collected with different amounts of Mn-precursors (denoted as the precursor molar ratio of Mn : Cu : Pb). (c) High-magnification SEM image and corresponding EDS element mapping images of the representative Cu–Mn-codoped $CsPb_2Br_5$.

Fig. 3 (a and b) PL spectra and UV-visible diffuse reflectance spectra, and XRD patterns of the undoped $CsPb_2Br_5$ and typical Cu–Zn-codoped and Cu–Cd-codoped $CsPb_2Br_5$ samples. (c) High-magnification SEM image and corresponding EDS element mapping images of the representative Cu–Cd-codoped $CsPb_2Br_5$.

microsheets obtained with a precursor Cu : Pb ratio of 5 : 20. The well-resolved interplanar distance of 0.301 nm in the undoped microsheets was assigned to the lattice (213) planes of tetragonal $CsPb_2Br_5$. Upon doping with Cu, the inter-fringe distance of 0.262 nm can be indexed to the (310) lattice planes. The elemental mapping of the Cu-doped sample illustrated in Fig. 2h–l indicated the uniform distributions of the Cs, Pb, Cu, and Br components throughout the $CsPb_2Br_5$ microsheets. The Cu : Cs : Pb : Br atomic ratio of the resulting Cu-doped sample was calculated to be approximately 0.17 : 1 : 2 : 5 according to the EDS analysis (Fig. S5 of the ESI†), in which the overall atomic ratio of Cs : Pb : Br agrees well with the stoichiometry ratio of $CsPb_2Br_5$.

We further tried co-doping $CsPb_2Br_5$ with Cu^{2+} and Mn^{2+} cations. The UV-visible DRS and PL spectra of the representative Cu–Mn-codoped samples are shown in Fig. 3a and S6 of the ESI.† The absorption features upon codoping with Cu^{2+} and Mn^{2+} cations are similar to those of the Cu-doped samples. By optimizing the amount of Mn^{2+} cations fed in the precursors, the PL intensity of the Cu–Mn-codoped $CsPb_2Br_5$ can be increased to around 8.0 fold relative to that of the undoped sample (see also Fig. S6a of the ESI†). The experimental XRD patterns (Fig. 2b) demonstrate that all the diffraction peaks are assigned to the tetragonal $CsPb_2Br_5$ phase (PDF # 00-025-0211) regardless of the amount of Mn-precursors. As noticed from the magnified view of the XRD pattern (Fig. S6c of the ESI†), the diffraction peak shifted towards a larger diffraction angle with the increase of the Mn amount fed in the precursors. An individual microsheet was selected for EDS elemental mapping analysis, confirming the uniform elemental distribution of Cu, Mn, Cs, Pb, and Br throughout the particle (Fig. 2c). The SEM images indicate
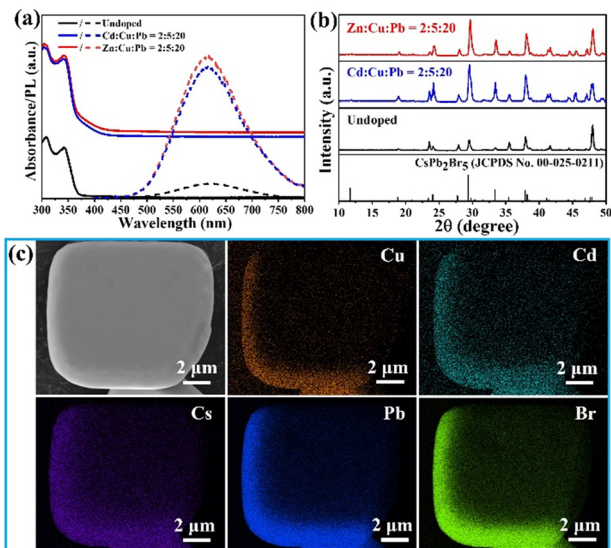
that the Cu–Mn-codoped $CsPb_2Br_5$ is microsheets in shape (Fig. S7 of the ESI†).

As a general protocol, we extended the synthetic procedure for codoping $CsPb_2Br_5$ with Cu/Zn and Cu/Cd, respectively. The optical properties, XRD patterns, morphologies, and elemental analyses of the representative samples are reported in Fig. 3 and S8–S11.† Both the Cu–Zn-codoping and Cu–Cd-codoping significantly enhanced the PL emission intensity. As shown in Fig. 3a, the PL intensity can be increased by around 9.1 and 8.4 fold upon codoping with Cu^{2+}/Zn^{2+} and Cu^{2+}/Cd^{2+} cations, respectively; in the meantime, the emission wavelength was maintained at around 618 nm (see also Fig. S8a and S11a of the ESI†). The XRD patterns of the Cu–Zn-codoped and Cu–Cd-codoped samples indicate that the crystal structure can remain as a tetragonal $CsPb_2Br_5$ phase (PDF # 00-025-0211) in both cases (Fig. 3b and S11b of the ESI†). EDS elemental mapping analysis on the codoped samples confirmed that the elements including Cu, Cd or Zn, Cs, Pb, and Br are uniformly distributed over the selected particles (Fig. 3c and S9†). The SEM images indicate that the morphology of the Cu–Zn-codoped $CsPb_2Br_5$ samples can be maintained as microsheets (Fig. S10†), while codoping with Cu^{2+} and Cd^{2+} leads to the formation of unregular cube-like particles (Fig. S11c of the ESI†).

Based on the above results, we conclude that the intensity of the PL spectra of the Cu-doped and various cation-codoped $CsPb_2Br_5$ samples is stronger than that of the undoped one. This can be explained by the boosted exciton recombination through a radiative pathway upon doping or codoping,[41] which consequently improves the emission performance. We noticed that no emissive materials can be formed when Zn^{2+} or Cd^{2+} is added alone (*i.e.*, without Cu^{2+})

in the precursors. Besides, doping $CsPb_2Br_5$ with Mn^{2+} alone leads to very weak emission compared to the Cu–Mn-codoped sample (Fig. S12 in the ESI†). These observations indicate that the introduction of Cu^{2+} cations played an important role in codoping, which might trigger the doping with other cations. Cation-codoping is more efficient in improving the emissive performance compared with doping, which might be due to a synergistic effect. Besides, overall, the diffraction peaks in the XRD patterns of the doped and codoped samples slightly shift to larger angles in comparison with that of undoped $CsPb_2Br_5$, which is in agreement with the Cu-doped $CsPbBr_3$[42] and Zn- and Ni-doped $CsPb_2Br_5$/$CsPbBr_3$ nanocrystals.[43] The slight shift of XRD peaks upon doping and codoping is due to the replacement of larger size Pb^{2+} cations by the smaller guest cations (*i.e.*, Cu^{2+}, Mn^{2+}, Zn^{2+} and Cd^{2+}), which led to a gradual shrinkage of the lattice.[44–46] Doping a host material with guest cations involves either interstitial dopants or substitutional dopants. It was reported that substitution with Cu^{2+} cations led to a negative shift of the XRD peaks towards smaller angles instead of larger angles.[47]

Stability of the cation-doped and codoped $CsPb_2Br_5$

The stability of materials is of great importance for practical application and commercialization. Therefore, we investigated the stability of the typical Cu-doped and various cation-codoped $CsPb_2Br_5$ materials under different environments such as soaking in water, heat treatment at high temperatures, and exposure to ambient conditions. First of all, water tolerance tests were carried out by immersing the various powder samples in water under ambient conditions. Fig. 4 and S13–S15 in the ESI† report the PL spectra, XRD patterns and SEM images of the Cu-doped and various cation-codoped $CsPb_2Br_5$ samples collected after immersion in water for different periods of time. Two unique features can be noticed from the evolution of optical spectra. First, in all cases, an additional shoulder peak of PL spectra emerged at around 480 nm besides the original orange-red emission at around 618 nm, as the soaking time was prolonged (Fig. 4a and b, see also Fig. S13 of the ESI†). This shoulder peak became relatively stronger in intensity compared with that of the peak at around 618 nm. Second, in all cases, the orange-red emission was enhanced at the early stage of the immersion in water. For example, the relative PL intensity at around 618 nm of the Cu-doped sample increased by 45.8% after soaking in water for 10 days compared with the initial PL intensity, which is superior to the previously reported $CsPb_2Br_5$-based heterostructure.[48] Even after 30 days of immersion in water, the intensity can maintain 67.8% of the initial intensity (green curve in Fig. 4a). Similar PL spectral evolution of the various cation-codoped samples over immersion time was observed (Fig. 4b and S13 of the ESI†). For example, the orange-red emission of the Cu–Zn-codoped $CsPb_2Br_5$ can be increased by around 36.9% after
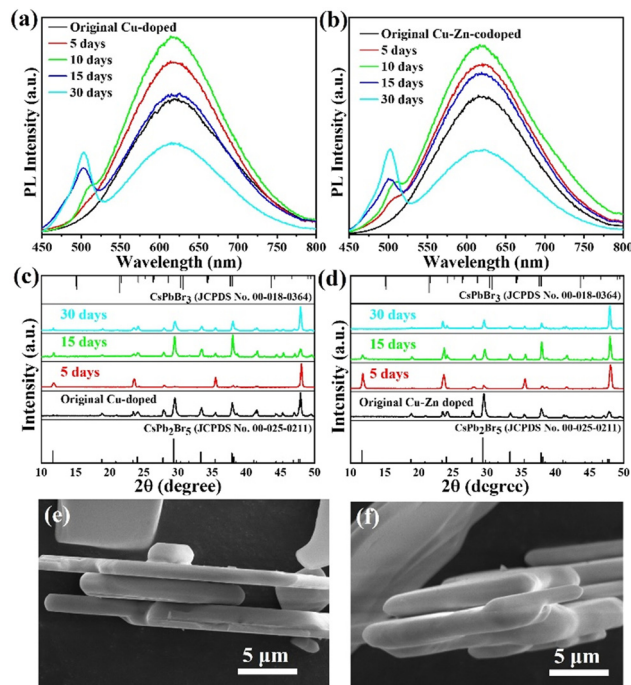

Fig. 4 Stability analyses of the representative Cu-doped and Cu–Zn-codoped $CsPb_2Br_5$ samples when immersed in water for different times. (a and b) The evolution of PL spectra of Cu-doped (a) and Cu–Zn-codoped $CsPb_2Br_5$ samples over immersion time. (c and d) XRD patterns of Cu-doped (c) and Cu–Zn-codoped $CsPb_2Br_5$ samples (d) soaked in water for different periods of time. (e and f) SEM images of the Cu-doped (e) and Cu–Zn-codoped $CsPb_2Br_5$ (f) soaked in water for 5 days.

immersion in water for 10 days (green curve in Fig. 4b). The XRD patterns of the various samples immersed in water for different times are reported in Fig. 4c and d and Fig. S14 of the ESI.† Overall, the main diffraction peaks corresponding to the $CsPb_2Br_5$ phase can be maintained even after soaking for 30 days, indicating that the sample can preserve its main crystal phase. No impurity diffraction peaks can be observed except that a diffraction peak at 2θ of 11.8° indexed to the (002) plane of $CsPb_2Br_5$ was detected in the intermediates (*e.g.*, sample immersed in water for 5 days). As shown from the SEM images (Fig. 4e and f and S15 of the ESI†), the morphology of the Cu-doped, Cu–Zn-codoped and Cu–Mn-codoped microsheets can be maintained after soaking in water for 5 days. All the above results indicate that the doped and codoped $CsPb_2Br_5$ materials display excellent stability against immersion in water for up to 15 days.

The thermal stability tests were carried out by monitoring the variation of the PL intensity and SEM images of the samples before and after treatment at different temperatures for 2 h under ambient conditions (Fig. 5 and S16 and S17 of the ESI†). It is noteworthy that the PL intensity of the Cu-doped and the various cation-codoped $CsPb_2Br_5$ samples was strengthened when treated at 100 °C for 2 h, by preserving the orange-red emission wavelength (Fig. 5a and b and S16 of the ESI†) and the
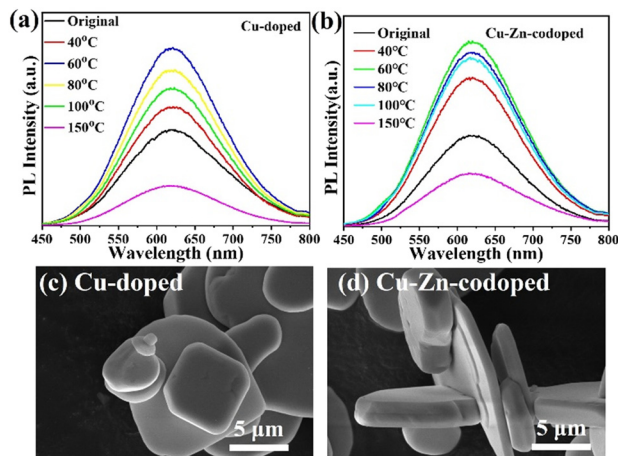
Fig. 5 (a) Thermal stability analyses of the Cu-doped and Cu–Zn-codoped $CsPb_2Br_5$ samples. (a and b) The PL spectra of Cu-doped (a) and Cu–Mn-codoped $CsPb_2Br_5$ samples (b) when treated at different temperatures for 2 h. (c and d) SEM images of the Cu-doped (c) and Cu–Zn-codoped $CsPb_2Br_5$ (d) after treatment at 80 °C for 2 h.

overall morphology (Fig. 5c and d and S17 of the ESI†). Significantly, the PL intensity was increased by 84.3% after treatment at 60 °C compared to the PL intensity of the untreated Cu-doped $CsPb_2Br_5$ (Fig. 5a, blue curve). Even at 100 °C, the PL intensity is around 1.42 times that of the untreated sample (green curve in Fig. 5a). Similar evolution of PL intensity over annealing temperature can be noticed for the various cation-codoped $CsPb_2Br_5$ samples. For instance, 2.1 times of the initial PL intensity can be achieved after treatment at 60 °C for 2 h regarding the Cu–Zn-codoped $CsPb_2Br_5$ (green curve in Fig. 5b). As confirmed by SEM observation, the morphology can be retained in the meantime (Fig. S17b of the ESI†). As further noticed from Fig. S18 of the ESI,†

the emission intensity can be enhanced at the early stage when the samples are exposed to an ambient environment, confirming the good stability of the various cation-doped and codoped $CsPb_2Br_5$ materials.

Scalability and reproducibility of the doped $CsPb_2Br_5$

The present technique can be readily extended to large-scale synthesis since it requires no specialized and expensive devices. The scalability was confirmed by reproducing Cu-doped $CsPb_2Br_5$ with 20-fold amounts of the related precursors and solvent relative to those in small-scale synthesis. Fig. 6 reports the corresponding characterization results of the representative large-scale synthesized Cu-doped $CsPb_2Br_5$. The PL spectrum displays a broad PL peak at around 618 nm (Fig. 6a). The synthesis reaction allowed for the generation of gram-scale orange-red emissive Cu-doped $CsPb_2Br_5$ powder (Fig. 6b), confirming the scalability of the present synthetic approach. The XRD analysis confirms the formation of the tetragonal $CsPb_2Br_5$ phase (Fig. 6c). The SEM image indicates that the Cu-doped $CsPb_2Br_5$ is microsheets (Fig. 6d). All these results are in agreement with those of the small-scale synthesized Cu-doped sample as discussed in the previous sections. The photoluminescence quantum yield (PLQY) of the Cu-doped $CsPb_2Br_5$ was tested to be 15.98%, which is lower than that of orange emissive $CsPb_2Br_5$ nanocrystals with a small particle size of around 3.87 nm and a PLQY of 23.8%.[37]

A mixture of the as-synthesized orange-red emissive $CsPb_2Br_5$, commercial green phosphors Ce:Ga-YAG, and blue $BaMgAl_{10}O_{17}:Eu^{2+}$ powders was blended with polydimethylsiloxane (PDMS) to form a viscous colloid dispersion. The dispersion was then coated onto a GaN UV chip emitting at 365 nm to achieve a typical WLED. Fig. 6e reports the CIE chromaticity diagram plotted from the
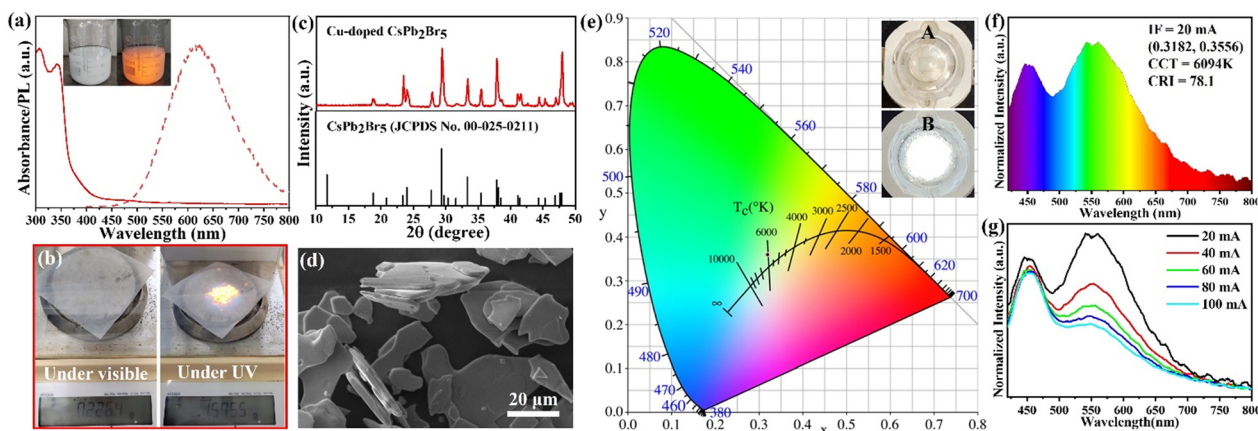

Fig. 6 Characterization results of the Cu-doped $CsPb_2Br_5$ achieved *via* large-scale synthesis: (a) PL and UV-visible diffuse reflectance spectra. (b) Photographs of Cu-doped $CsPb_2Br_5$ powder on an electronic balance displaying gram-scale synthesis. (c) XRD pattern. (d) SEM image of the large-scale synthesized sample. (e) CIE chromaticity diagram of the white LED (WLED) device fabricated with the as-synthesized orange-red Cu-doped $CsPb_2Br_5$, green Ce:Ga-YAG, and blue $BaMgAl_{10}O_{17}:Eu^{2+}$. Insets provide the digital photographs of the as-fabricated WLED lamp (A) and the lamp displayed under working conditions (B). (f) EL spectrum of a WLED device under a working current of 20 mA. (g) Output spectra of WLEDs at different currents.

electroluminescence spectrum of the corresponding WLED device. Fig. 6f displays the spectra of the WLED operating at 20 mA. The CIE color coordinate, correlated color temperature (CCT) and color rendering index (CRI) values of the WLED device are (0.3182 0.3556), 6094 K, and 78.1, respectively. Under 20 mA, the luminous efficacy of the WLED is 1.25 lm W^{-1}. Fig. 6g reports the EL spectra of the WLED driven by different working currents, which indicates that the relative intensity ratios of the orange-red peak and blue/green peaks decreased as the diode currents increased from 20 to 100 mA.

Conclusions

In summary, we developed a facile RT aqueous phase synthetic approach to prepare orange-red emissive cation-doped and codoped $CsPb_2Br_5$ materials with enhanced stability. In comparison with the undoped $CsPb_2Br_5$ microsheets, the Cu-doped, Cu–Mn-codoped, Cu–Zn-codoped, and Cu–Cd-codoped $CsPb_2Br_5$ display a significant enhancement in PL intensity by maintaining the overall emission wavelength at around 618 nm. By optimization of the types and amounts of dopants (*i.e.*, Cu^{2+}, Mn^{2+}, Zn^{2+}, and Cd^{2+} cations) in the precursors, the PL intensity of the resulting samples can be increased to around 9.1 times compared to that of undoped $CsPb_2Br_5$. Besides, relative to the as-synthesized fresh samples, the intensity of the orange-red emission of all the doped and codoped $CsPb_2Br_5$ samples can be increased at the early stage after immersion in water, or treatment at temperatures below 100 °C, indicating excellent aqueous and thermal stability. This work would offer a facile and scalable synthetic approach at RT for orange-red emissive cation-doped/codoped Cs–Pb–Br materials with enhanced optical performances and excellent environmental stability.

Data availability

All relevant data are within the main text and ESI.†

Conflicts of interest

There are no conflicts to declare.

Acknowledgements

References

1 M. Simenas, A. Gagor, J. Banys and M. Maczka, *Chem. Rev.*, 2024, **124**, 2281–2326.

2 K. Wang, G. Xing, Q. Song and S. Xiao, *Adv. Mater.*, 2021, **33**, 2000306.

3 M. Cao, Y. Damji, C. Zhang, L. Wu, Q. Zhong, P. Li, D. Yang, Y. Xu and Q. Zhang, *Small Methods*, 2020, **4**, 2000303.

4 Z. Zhang, Y. Zhu, W. Wang, W. Zheng, R. Lin and F. Huang, *J. Mater. Chem. C*, 2018, **6**, 446–451.

5 G. Murugadoss, R. Thangamuthu, S. M. Senthil Kumar, N. Anandhan, M. Rajesh Kumar and A. Rathishkumar, *J. Alloys Compd.*, 2019, **787**, 17–26.

6 R. Wang, Z. Li, S. Li, P. Wang, J. Xiu, G. Wei, H. Liu, N. Jiang, Y. Liu and M. Zhong, *ACS Appl. Mater. Interfaces*, 2020, **12**, 41919–41931.

7 M. I. Saidaminov, O. F. Mohammed and O. M. Bakr, *ACS Energy Lett.*, 2017, **2**, 889–896.

8 T. Zhang, Z. Chen, Y. Shi and Q.-H. Xu, *Nanoscale*, 2019, **11**, 3186–3192.

9 H. Yang, Y. Zhang, J. Pan, J. Yin, O. M. Bakr and O. F. Mohammed, *Chem. Mater.*, 2017, **29**, 8978–8982.

10 L. Ruan, J. Lin, W. Shen and Z. Deng, *Nanoscale*, 2018, **10**, 7658–7665.

11 G. Li, H. Wang, Z. Zhu, Y. Chang, T. Zhang, Z. Song and Y. Jiang, *Chem. Commun.*, 2016, **52**, 11296–11299.

12 R. Zhi, J. Hu, S. Yang, C. Perumal Veeramalai, Z. Zhang, M. I. Saleem, M. Sulaman, Y. Tang and B. Zou, *J. Alloys Compd.*, 2020, **824**, 153970.

13 S. K. Balakrishnan and P. V. Kamat, *Chem. Mater.*, 2018, **30**, 74–78.

14 M. Li, X. Zhang, T. Dong, P. Wang, K. Matras-Postolek and P. Yang, *J. Phys. Chem. C*, 2018, **122**, 28968–28976.

15 S. Lou, Z. Zhou, T. Xuan, H. Li, J. Jiao, H. Zhang, R. Gautier and J. Wang, *ACS Appl. Mater. Interfaces*, 2019, **11**, 24241–24246.

16 P. Gao, Z. Cui, X. Liu, Y. Wu, Q. Zhang, Z. Wang, Z. Zheng, H. Cheng, Y. Liu, Q. Li, B. Huang and P. Wang, *Chem. – Eur. J.*, 2022, **28**, e202201095.

17 Y. Zhang, Y. Ma, Y. Wang, X. Zhang, C. Zuo, L. Shen and L. Ding, *Adv. Mater.*, 2021, **33**, 2006691.

18 X. Dong, E. Acheampong Tsiwah, T. Li, J. Hu, Z. Li, Y. Ding, Z. Deng, W. Chen, L. Xu, P. Gao, X. Zhao and Y. Xie, *Nanoscale*, 2019, **11**, 7903–7912.

19 Y. Ding, T. Li, X. Li, E. A. Tsiwah, C. Liu, P. Gao, T. Zeng, Y. Chen, X. Zhao and Y. Xie, *CrystEngComm*, 2019, **21**, 2388–2397.

20 S. Li, H. Lin, C. Chu, C. Martin, W. MacSwain, R. W. Meulenberg, J. M. Franck, A. Chakraborty and W. Zheng, *ACS Nano*, 2023, **17**, 22467–22477.

21 Y. Zhang, C. Fan, D. Ge, Q. Zhang, S. Huang, G. Zhang and J. Su, *J. Alloys Compd.*, 2024, **973**, 172932.

22 Y.-T. Zeng, Z.-R. Li, S.-P. Chang, A. Ansay, Z.-H. Wang and C.-Y. Huang, *Nanomaterials*, 2022, **12**, 759.

23 S. Sun, M. Lu, J. Guo, F. Zhang, P. Lu, Y. Fu, X. Bai, Z. Shi, Z. Wu, W. W. Yu and Y. Zhang, *Chem. Eng. J.*, 2022, **433**, 133556.

24 S. Xue, H. Mao, J. Li, X. Sun, Z. Gong, B. Fan, G. Shao, H. Wang, H. Xu, R. Zhang and H. Lu, *Ceram. Int.*, 2023, **49**, 35202–35212.

25 D. Kushavah, A. Mushtaq and S. K. Pal, *J. Phys. Chem. C*, 2023, **127**, 20014–20025.

26 J. Qiu, H. Zhao, Z. Mu, J. Chen, H. Gu, C. Gu, G. Xing, X. Qin and X. Liu, *Nano Lett.*, 2024, **24**, 2503–2510.

27 T. Li, Y. Ding, S. Kareem, F. Qiao, G. Ali, C. Ji, X. Zhao and Y. Xie, *J. Colloid Interface Sci.*, 2019, **552**, 101–110.

28 H. Dong, S. Kareem, X. Gong, J. Ruan, P. Gao, X. Zhou, X. Liu, X. Zhao and Y. Xie, *ACS Appl. Mater. Interfaces*, 2021, **13**, 23960–23969.

29 Y. Hu, S. Kareem, H. Dong, W. Xiong, S. Tian, J. Shamsi, L. Li, X. Zhao and Y. Xie, *ACS Appl. Nano Mater.*, 2021, **4**, 6306–6315.

30 Y. Hu, H. Dong, A. R. Tapa, J. Shamsi, J. S. Shayeh, A. Trokourey, B. Liu, X. Zhao and Y. Xie, *ACS Appl. Nano Mater.*, 2023, **6**, 2538–2548.

31 I. Dursun, M. De Bastiani, B. Turedi, B. Alamer, A. Shkurenko, J. Yin, A. M. El-Zohry, I. Gereige, A. AlSaggaf, O. F. Mohammed, M. Eddaoudi and O. M. Bakr, *ChemSusChem*, 2017, **10**, 3746–3749.

32 S. Li, F. Wang, S. Dong, H. Dou, T. Wang and H.-E. Wang, *Chem. Commun.*, 2024, **60**, 4679–4682.

33 X. Tang, S. Han, Z. Zu, W. Hu, D. Zhou, J. Du, Z. Hu, S. Li and Z. Zang, *Front. Phys.*, 2018, **5**, 69.

34 K.-H. Wang, L. Wu, L. Li, H.-B. Yao, H.-S. Qian and S.-H. Yu, *Angew. Chem., Int. Ed.*, 2016, **55**, 8328–8332.

35 L. Ruan, W. Shen, A. Wang, A. Xiang and Z. Deng, *J. Phys. Chem. Lett.*, 2017, **8**, 3853–3860.

36 T. Chen, C. Wang, X. Xing, Z. Qin, F. Qin, Y. Wang, M. K. Alam, V. G. Hadjiev, G. Yang, S. Ye, J. Yang, R. Wang, S. Yue, D. Zhang, Z. Shang, F. C. Robles-Hernandez, H. A. Calderon, H. Wang, Z. Wang and J. Bao, *Small*, 2022, **18**, 2105009.

37 Y. Yin, Y. Liu, G. Cao, Z. Lv, H. Zong, Y. Cheng, Q. Dong, C. Liu, M. Li and B. Zhang, *J. Alloys Compd.*, 2023, **947**, 169439.

38 V. A. Pustovarov, I. N. Ogorodnikov, N. S. Bastrikova, A. A. Smirnov, L. I. Isaenko and A. P. Eliseev, *Opt. Spectrosc.*, 2006, **101**, 234–244.

39 X. Tang, Z. Hu, W. Yuan, W. Hu, H. Shao, D. Han, J. Zheng, J. Hao, Z. Zang, J. Du, Y. Leng, L. Fang and M. Zhou, *Adv. Opt. Mater.*, 2017, **5**, 1600788.

40 C. Qin, T. Matsushima, A. S. D. Sandanayaka, Y. Tsuchiya and C. Adachi, *J. Phys. Chem. Lett.*, 2017, **8**, 5415–5421.

41 J. Deng, J. Xun, W. Shen, M. Li and R. He, *ACS Appl. Nano Mater.*, 2021, **4**, 9213–9222.

42 B. Wang, L. Liu, B. Liu, J. Li, B. Cao, Z. Zhao and Z. Liu, *Phys. B*, 2020, **599**, 412488.

43 J. Deng, Y. Cui, Z. Jiang, R. Du, L. Yang, X. Zhang, R. He and J. Zhang, *J. Mater. Chem. C*, 2022, **10**, 18336–18342.

44 H. Dong, J. Kong, F. Wang, C. Zhang, J. Chen, L. Li, C. Wang, Y. Sun, Y. Jin, F. Qiao and W. Shen, *J. Alloys Compd.*, 2022, **902**, 163844.

45 J. Ghosh, M. Hossain and P. K. Giri, *J. Colloid Interface Sci.*, 2020, **564**, 357–370.

46 S. Zhou, Y. Zhu, J. Zhong, F. Tian, H. Huang, J. Chen and D. Chen, *Nanoscale*, 2019, **11**, 12465–12470.

47 H. Bian, T. Liu, D. Li, Z. Xu, J. Lian, M. Chen, J. Yan and S. Frank Liu, *Chem. Eng. J.*, 2022, **435**, 135071.

48 J. Yao, T. Yao, K. Zhang, W. Fan, Z. Yang, L. Xu, S. Wang and J. Song, *Mater. Chem. Front.*, 2024, **8**, 1628–1635.